Milestones in Physics (26)

SLS 2.0 – The upgrade of the Swiss Light Source

Philip R. Willmott, Paul Scherrer Institute, CH-5232 Villigen, philip.willmott@psi.ch

The Swiss Light Source (SLS) has been operational since 2001. In the last two decades, unique and groundbreaking scientific programs and methods have been developed at the SLS in fields as diverse as macromolecular biology, imaging, and the electronic structure and behaviour of novel and complex materials. These achievements have been largely underpinned by the excellent performance of the electron accelerator and storage ring, which was considered the benchmark in this field until well into the second decade of this century. Nonetheless, with the advent of novel technologies in accelerator physics and the consequent emergence of the next generation of storage-ring facilities, known as diffraction-limited storage rings (or DLSRs), it has now become imperative to upgrade the SLS in like manner. The general features of DLSRs, the characteristics of the new SLS 2.0 machine, and the scientific opportunities it will offer are the subject of this in-part didactic article.

I. Introduction

The Swiss Light Source (SLS) has been serving the international scientific community since 2001 in scientific endeavours as diverse as bioimaging, macromolecular biology, novel electronic materials, nanomagnetism, catalysis and energy research, and cultural heritage, to name just some examples. Indeed, two Nobel prizes were awarded for discoveries enabled by experimental data obtained at the SLS [1–4].

The SLS has been a highly attractive research tool for many reasons, including the reliability and stability of the performance of the storage ring. A decade after its inauguration, the horizontal electron emittance value of 5.6 nm rad (the concept of emittance is described below) was considered to be a benchmark for storage-ring facilities, boasting horizontal and vertical electron emittances that approached the theoretical limit, given the machine parameters and contemporary magnet-lattice technology [1]; moreover it was with the SLS that regular so-called 'top-up' operation was first implemented – this allows small injections of the order of a percent of the total current at intervals measured in a few minutes, instead of the previous approach of letting the electron beam current decay by a few tens of percent over hours before injection. This has the advantage of maintaining an almost constant thermal load on the beamline components, in particular mirrors and monochromators, thereby permitting much more stable operation.

Nonetheless, a quantum leap in storage-ring performance was promised by innovations in beam dynamics theory, magnet fabrication and vacuum technologies that emerged in the first decade of this century [7], resulting in the emergence of fourth-generation storage-ring facilities known as diffraction-limited storage rings (DLSRs). There are already three operational DLSRs, namely MAX-IV in Lund, Sweden, the ESRF-EBS in Grenoble, France, and SIRIUS, in Campinas, Brazil, while several more are in the planning or active upgrade stage.

To appreciate the approximately two orders of magnitude improvement in performance promised by these developments, the concept of the figure-of-merit for synchrotrons called the 'brightness', or 'brilliance', must be understood. We thus begin with a short exposition on machine physics.

II. Some Basic Storage-Ring Machine Physics

A. Brightness and emittance

Brightness encapsulates the most important parameters of synchrotron radiation in a single figure of merit (see Figure 1). It is defined as the flux of photons produced per unit time and in a defined bandwidth from a source exhibiting a certain source area and divergence. It is specifically given by

$$\mathcal{B}(h\nu) = \frac{\text{ph / s}}{\sigma_x \sigma_y \times \sigma'_x \sigma'_y \times 0.1\,\%\,\text{BW}} \quad (1),$$

where by $\sigma_{x,y}$ (in mm) and $\sigma'_{x,y}$ (in mrad) are the standard deviations of the beam profiles of the source size and divergence, respectively, in the x- and y-directions. An undulator source at third-generation synchrotron facilities can expect to deliver brilliances of the order of 10^{19} to 10^{20} ph / (s · mm^2 · mrad^2 · 0.1 % BW).

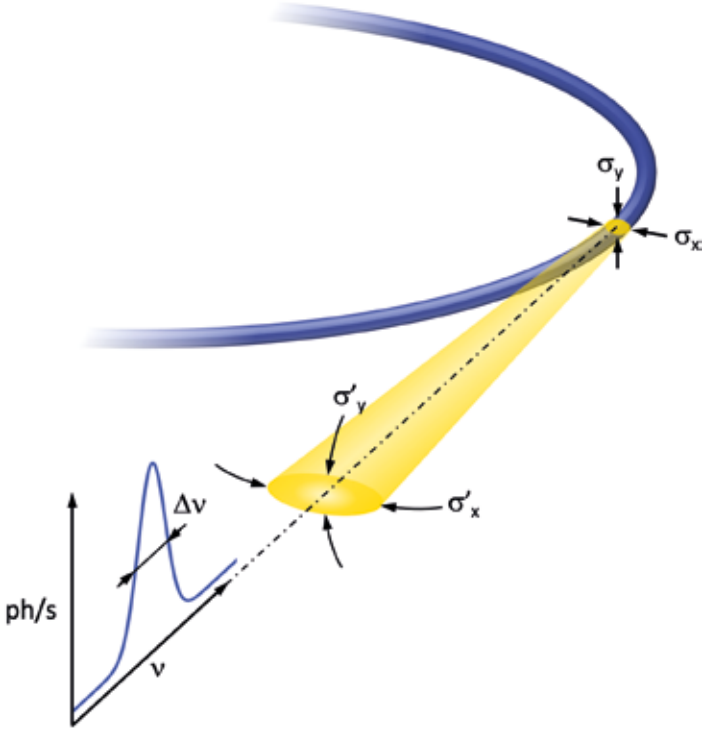

Figure 1. Schematic of the parameters determining brilliance, see Equation 1. The root-mean-square (RMS) source sizes $\sigma_{x,y}$ and divergences $\sigma'_{x,y}$ in the planes perpendicular to the direction of radiation define the emittance; the relative bandwidth is given by the bandwidth $\Delta\nu$ divided by the central frequency ν, delivering a flux given in ph s^{-1}. Adapted from [8], with permission of John Wiley & Sons.

1 The original SLS design was in fact what today is called a multibend achromat lattice. This design was developed between 1993 and 1996 [5, 6]. The final design was changed to a triple-bend achromat, as no suitable multibend solution could be found at the time.

The combined quantity of source size and divergence found in the denominator of the expression for brilliance is referred to as emittance, ε. The horizontal emittance in the orbital plane, $\varepsilon_x = \sigma_x \sigma'_x$ is generally larger than the emittance in the vertical plane $\varepsilon_y = \sigma_y \sigma'_y$.

The total emittance in any one plane is a convolution of the electron emittance, ε^e, which can be tuned according to the storage-ring design, and the photon emittance, ε^p, which is a fundamental property defined solely by the photon energy. It can be shown that the source size and divergence of radiation from an undulator source of length L, ignoring contributions from the electron beam, are given by

$$\sigma^p = \frac{\sqrt{\lambda L}}{4\pi} \quad (2);$$

$$\sigma'^p = \sqrt{\lambda / L} \quad (3),$$

and hence

$$\varepsilon^p = \frac{\lambda}{4\pi} \quad (4).$$

The ratio σ^p / σ'^p is referred to as the photonic beta function $\beta^p = L/4\pi$, which has units of length and is independent of the radiation wavelength. Analogously, the beta function of the electron beam is given by $\beta^e = \sigma^e / \sigma'^e$; this can, however, be manipulated using electron optics.

It is thus important to match the storage ring parameters at each source point to that source's design. The flux of a beamline is simply the brilliance multiplied by the total emittance, and thus has dimensions of [ph/s/0.1 % bandwidth]. It is briefly noted that for some synchrotron techniques, flux on the sample is more important than the brilliance, particularly for those that do not require the smallest focus, or don't exploit the coherent properties of the beam.

In the hard x-ray regime, for which $\lambda \sim 1$ Å (12-keV photons), the photon emittance, according to Equation 4 is of the order of 10 pm rad. Even for photon energies in the regime of 1 keV, $\varepsilon^p \sim 100$ pm rad, and hence the photon emittance is between one and two orders of magnitude smaller than the electron emittance in third-generation facilities. The performance of third-generation facilities is thus primarily determined by the electron emittance.

B. Multibend achromats and the diffraction limit

The electron emittance is determined by the so-called radiation equilibrium: like in a spectrometer, the bending magnets forming the storage-ring lattice deflect particles depending on their energy spread – an effect called dispersion. The quantum nature of photon emission introduces a stochastic spread of individual electron energies, which is then translated into a spatial spread in the orbital plane through dispersion.

On the other hand, continuous energy loss to radiation in combination with acceleration of the electrons in the radio frequency cavities of the storage ring provides damping of the energy fluctuations [8]. Finally, the emittance of the electron beam is given by the competing effects of radiation damping and quantum excitation, forming an equilibrium, which is dictated by the structure of the magnet lattice.

Obviously, in order to adjust the equilibrium beam emittance to low values requires that the dispersion remains small inside the bending magnets. This means one should rather use many small bending magnets instead of a few big ones, in order to prevent the dispersion growing to large values inside the magnet.

Thus, the defining feature of fourth-generation synchrotron facilities is the employment of so-called multibend achromats (MBAs) in the arc sectors of the storage ring. What is meant by this term? Classically, the arc sectors of synchrotrons, that is, the regions which are responsible for bending the electron beam into a closed path, are served by so-called double-bend achromats [2].

A double-bend achromat (DBA), as depicted in Figure 2, uses two bending-magnet dipoles separated by focusing quadrupole magnets. This has in the past been the standard system to suppress dispersion in the straight sections at third-generation synchrotrons. A multibend achromat is similar, but uses several small DBAs in a row, typically between 5 and 9, to execute a given arc angle. An MBA with M dipoles contains (M – 1) DBA cells (Figure 2 bottom).

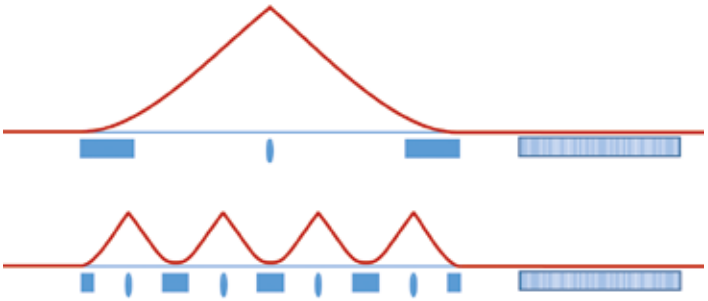

Figure 2. Schematics of a double bend achromat (DBA) and multibend achromat (MBA). The red line indicates the dispersion, which is refocused by magnetic lenses (quadrupoles) in order to minimize it inside the dipoles and to suppress it in the straight sections, where the undulators are located. From [9], with permission from the Swiss Society for Photon Science.

Limiting the dispersion growth inside the bending magnets enables a dramatic reduction in emittance: the *minimum* horizontal electron emittance theoretically attainable by an MBA structure is found to be proportional to the third power of the bending angle θ of the dipoles used in the MBA [8]. Precisely,

$$\varepsilon_x^e = \frac{C_q \gamma^2}{12\sqrt{15}\, J_x} \theta^3 \quad (5),$$

where $\gamma = \mathcal{E} / m_e c^2$ is the ratio of the storage ring energy to the electron rest-mass energy, and $C_q = 3.832 \times 10^{-13}$ m. The parameter J_x in the denominator depends on the distribution of radiation damping to transverse and longitudinal dimensions and typically has values between 1 and 2.

Note that ε_x^e depends on the square of the storage-ring energy. Despite this, the upgrade of the SLS includes an *increase* in this parameter from $\mathcal{E}$ = 2.4 to 2.7 GeV [10, 11], as this will facilitate access to photon energies well in excess of 40 keV, which is especially interesting for both imaging and chemical spectroscopies, two areas of research in which the SLS has historically been a leading player.

2 Some third-generation facilities, notably the SLS until its upgrade, use a triple bend achromat, but this is a detail that need not concern us here.

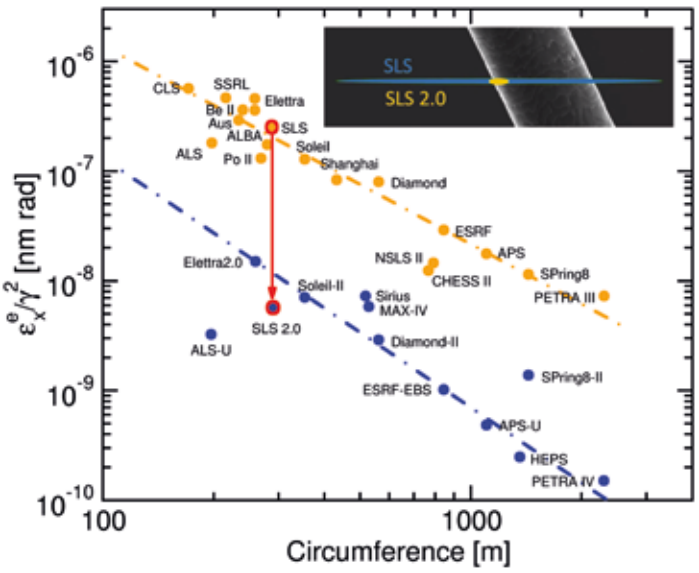

Figure 3. Plot of horizontal electron emittances weighted by the square of the storage-ring energy as a function of ring circumference (see Equation 5), for both a selection of third- (orange data points) and fourth-generation (blue) synchrotrons. Note the approximately fortyfold improvement in the weighted emittance for the SLS 2.0 upgrade, highlighted in red. The inset shows the cross-sections of the electron beams at SLS and SLS 2.0 compared to a typical human hair. From [9], with permission from the Swiss Society for Photon Science.

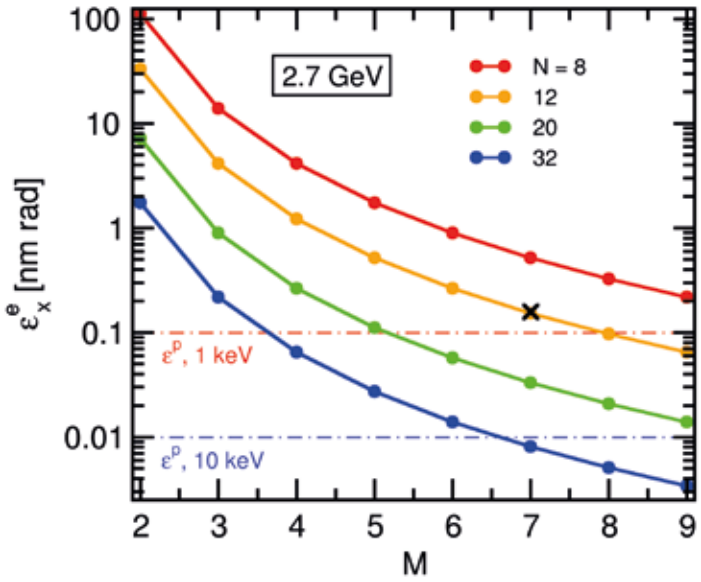

Figure 4. Plot of the theoretically optimal horizontal electron emittance ε_x^e as a function of the number of straights N in a 2.7-GeV synchrotron ring and number of dipoles M within a single arc sector, according to Equation 6. Values for N = 12, 20, and 32 were selected, as these correspond to SLS 2.0, MAX-IV, and ESRF-EBS, respectively. Also included as dot-dash lines are the fundamental photon emittances for 1 and 10-keV photons, given by Equation 4, and the position of SLS 2.0, labelled as the black X. From [9], with permission from the Swiss Society for Photon Science.

The path to low emittance by building a lattice from many small magnets became viable once miniaturization of accelerator components became feasible, in particular with regards to the precision of magnet construction and distributed pumping via so-called 'nonevaporable getter' (NEG) coatings on the inner surfaces of the narrow-cross-section vacuum vessels containing the circulating electrons.

For a storage ring containing N arcs of M dipoles each, the bending angle per dipole is simply $\theta = 2\pi/N(M-1)$, and Equation 5 becomes

$$\varepsilon_x^e = \frac{2C_q\gamma^2\pi^3}{3\sqrt{15}\,J_x}\frac{1}{N^3(M-1)^3} \qquad (6)$$

$$\Rightarrow \varepsilon_x^e\,[\mathrm{nm\,rad}] = 7834\frac{(\mathcal{E}\,[\mathrm{GeV}])^2}{J_x}\frac{1}{N^3(M-1)^3} \qquad (7).$$

Therefore, SLS 2.0, for which $N = 12$ and $M = 7$, has a theoretical ultimate horizontal electron emittance of 153 pm rad (for $J_x = 1$). The actual goal is ε_x^e = 157 pm rad (Figure 3) [11].

From our expression given in Equation 4, we can calculate that radiation with the same emittance ε^p as ε_x^e will, for SLS 2.0, have a wavelength of 19.73 Å, equating to a photon energy of approximately 630 eV; these are referred to as the 'diffraction-limited wavelength' λ_{DL} and 'diffraction-limited energy' $h\nu_{DL}$, respectively. For photon energies much lower than this, the photon contribution to the total emittance dominates, and no substantial gain is made by attempts to improve the electron emittance further [3]. This is the meaning of diffraction-limited storage rings – their performance is limited, at least for photon energies below that for which $\varepsilon^p = \varepsilon_x^e$, by fundamental diffraction phenomena associated with the x-ray sources. We summarize this in Figure 4.

3 Note that, for third-generation facilities, the 'diffraction-limited photon energy' is of the order of 20 eV.

The electron emittance is a constant around the storage ring for a given magnet lattice. In the above, however, we have not considered how this is distributed between divergence and electron-beam size – do we want the electron beam to be very small but highly divergent (low β^e), or larger and more parallel (high β^e)? Importantly, although the electron emittance remains constant for a given ring, one can manipulate β^e using the electron optics such as the quadrupole magnets and the combined function magnets, which are magnets providing focusing and bending simultaneously. Now, because the total emittance is the convolution of the electron- and photon contributions, it is easy to demonstrate that the beta function of the electron emittance is optimized, and thereby the total emittance is minimized, when it equals that of the photon emittance, i.e., $L/4\pi$, that is, of the order of a few tens of cm, depending on the undulator length.

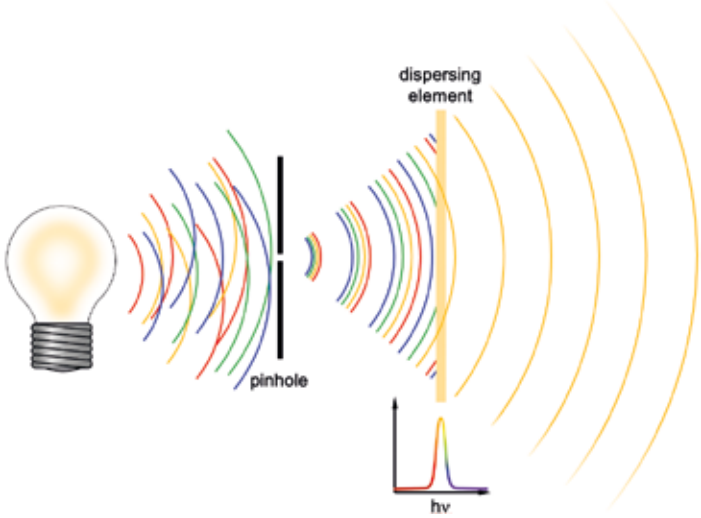

Figure 5. Coherent radiation can be extracted from a broadband, spatially extended source by the use of a pinhole and a dispersive element that selects a narrow band of wavelengths. Adapted from [8], with permission of John Wiley & Sons.

C. Coherence

To conclude this whistle-stop précis of the most important aspects of storage-ring and radiation parameters, we briefly discuss coherence. Within the figure of merit of brightness are the parameters that quantitatively define coherence – the emittance and the relative spectral bandwidth. Consider a broadband and spatially distributed source such as an incandescent light bulb (Figure 5). The source emittance can be reduced by placing a slit or pinhole in front of the source. This determines the 'spatial', or 'transverse' coherence. In the case of synchrotrons, the slit (or source) size is given by the transverse spatial extent of the beam. Even for soft x-ray sources below a few keV, this is dominated by the size of the electron beam, as this will be of the order of tens of microns or more, much larger than the radiation's wavelength, measured in nanometers or angstroms. The divergence is given by the Fourier transform of the source profile; accordingly, the full-width half-maximum (FWHM) subtended angle is approximately equal to the ratio of the wavelength to the beam FWHM, of the order of 10^{-4} rad for soft x-radiation. Secondly, a dispersive element such as a monochromator suppresses all radiation apart from a narrow bandwidth. Now, the radiation is both spatially and longitudinally (or temporally) coherent. Both the emittance and relative spectral bandwidth are included in the definition of brilliance.

The transverse coherence length at a distance R from a source of width D is given by

$$l_c^{(t)} = \frac{\lambda R}{2D} = \frac{\lambda R}{2\sqrt{\pi}\,\sigma_{x,y}} \quad (8).$$

Hence, in the orbital plane of the synchrotron, DLSRs have transverse coherence lengths of several hundred microns, up to two orders of magnitude larger than those typically found at third-generation facilities. This has a huge benefit both for lensless-imaging techniques such as ptychography [12, 13] that exploit the coherent part of the beam, and also those techniques that require both small divergence and a tight focus, such as in serial crystallography [14].

The 'temporal', or 'longitudinal' coherence length, determined by the degree of monochromacity, is given by

$$l_c^{(l)} = \frac{\lambda^2}{\Delta\lambda} \quad (9).$$

The temporal coherence length thus depends on any dispersive element in the beamline, particularly monochromators. A Si(111) double-crystal monochromator has an intrinsic relative bandwidth of approximately 1.4×10^{-4}, which, for 1-Å-radiation leads to $l_c^{(l)} \sim 1\ \mu$m. Note that DLSR technologies do not in themselves provide advantages in longitudinal coherence compared to third-generation facilities.

III. Sources at the SLS 2.0 Upgrade

A graphical summary of the expected brilliances of the x-ray sources at SLS 2.0 is provided in Figure 6, while further details of their parameters are listed in Table 1.

The six hard x-ray undulator beamlines are served by four U17s, one cryogenically-cooled U14 (also operational at the original SLS), and one high-temperature superconducting U10, while four hard x-ray bending-magnet beamlines have

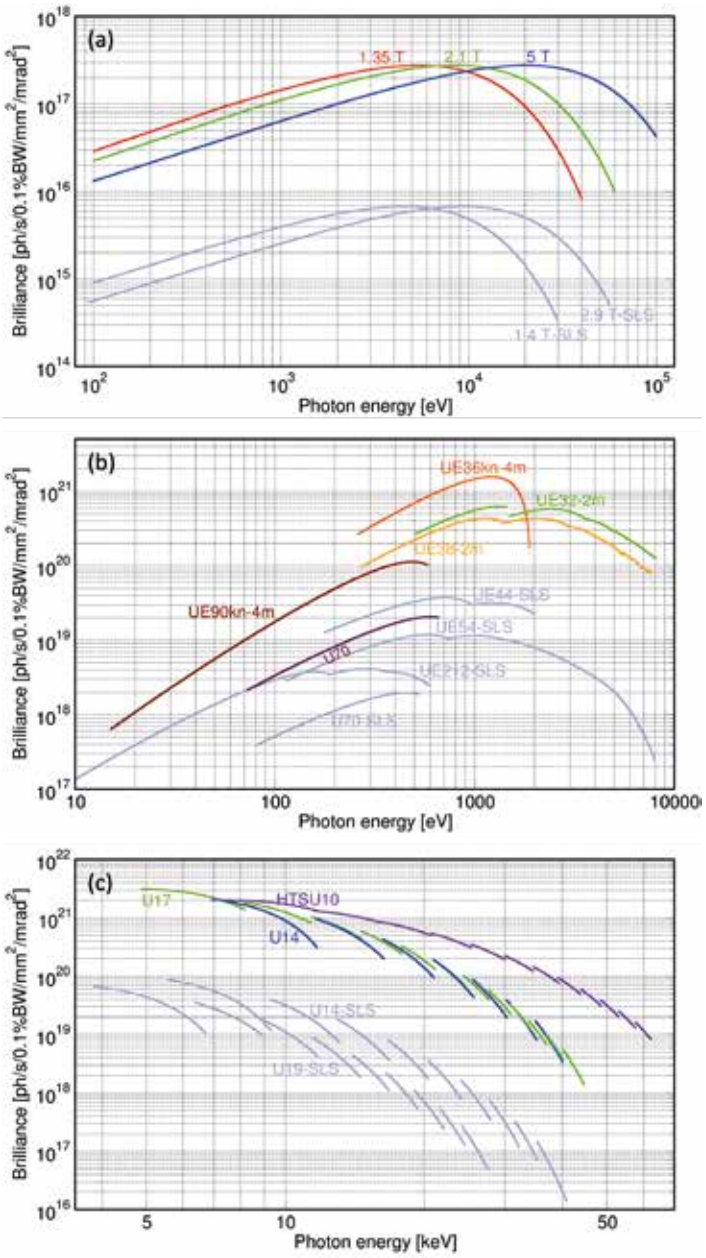

Figure 6. Brilliance curves of the SLS 2.0 sources for (a) bending magnets and superbends, (b) soft x-ray undulators, and (c) hard x-ray undulators. -kn suffix = knot magnet design; HTSU = high-temperature superconducting undulator; UE = elliptical undulator; two-digit suffices = undulator periodicity in mm. The performance of the previous sources installed in the 2.4-GeV storage ring are also shown in grey.

two warm superbends (2.1 T) and two superconducting superbends (5 T). The five remaining straights produce soft and tender x-rays, and are served by combinations of the elliptical undulators (UEXX).

An exciting aspect of the upgrade is that improvements in the brilliance also enable other innovations further down the technological chain, notably in the field of undulator development.

A. Hard x-ray undulators

The description of the interference phenomena that lead to the spectral output from undulators is given by

$$m\lambda_m(\theta) = \frac{\lambda_u}{2\gamma^2}\left(1 + \frac{K^2}{2} + \gamma^2\theta^2\right) \quad (10),$$

whereby λ_m is the wavelength of the m^{th} harmonic, λ_u is the

ID name	λ_u [mm]	$h\nu$-range [eV]	Length [m]	Polarization modes	ID beamlines
UE90kn	90	30 – 600	4.0	LH, LV, CL, CR	QUEST, XIL
U70	70	70 – 660	1.54	LH	XIL
UE38	38	250 – 8000	2.0	LH, LV, CL, CR	PHOENIX/X-Treme
UE36kn	36	270- 1900	4.0	LH, LV, CL, CR	SIM, ADRESS, QUEST
U17	16.8	4900 – 34000	3.0	LH	cSAXS, PXI, PXII, microXAS
CPMU14	14	7000 – 40000	1.68	LH	MS (ADDAMS)
HTSU10	10.5	7000 – 62000	1.0	LH	I-TOMCAT

Table 1. List of insertion devices, their relevant parameters, and the beamlines they serve. Insertion device names ending in 'kn' indicate knot-magnet configurations. LH = linear horizontal, LV = linear vertical, CL = left-circularly, CR = right-circularly.

periodicity of the undulator magnet array (typically measured in cm), and

$$K = 0.934\ \lambda_u[\mathrm{cm}]\, B_0[\mathrm{T}] \sim 1 \quad (11)$$

is the magnetic deflection parameter describing the ratio of the maximum angular excursion of the electron beam as it passes through the undulator's magnet array to the natural opening angle of the synchrotron radiation, which is itself equal to $1/\gamma$. The second term in the brackets, $\gamma^2\theta^2$, describes the contribution from off-axis radiation. This results in broad lobes on the low-energy flanks of the main undulator maxima (see the curve for the undulator spectrum for third-generation facilities in Figure 7).

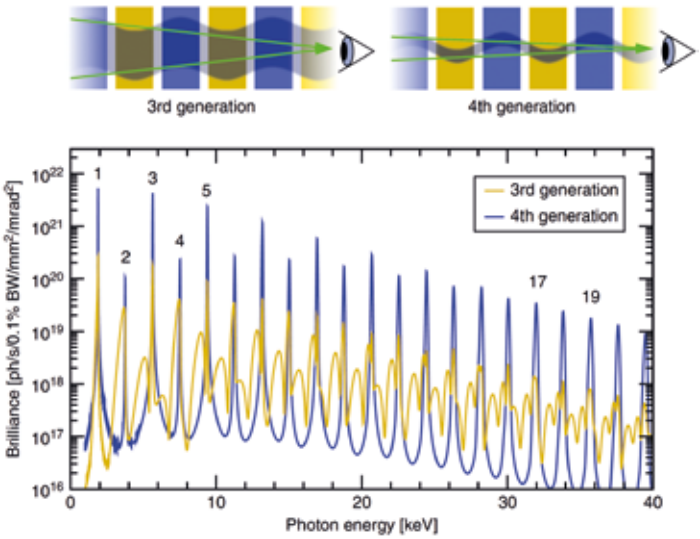

Figure 7. Comparison of the brilliance of hard x-ray undulator spectra at third- and fourth-generation facilities. Top: the width of the electron beam passing through an undulator at third-generation facilities is approximately two orders of magnitude larger than the oscillation amplitude, while at DLSRs, it might only be approximately ten times, or even less. Bottom: consequently, less off-axis radiation (given by Equation 10) is produced by undulators at DLSRs. Note also the enhanced brilliance at the spectral peaks for the DLSR. Both simulated spectra were generated for a U12 undulator (that is, λ_u = 12 mm) containing 120 magnet periods, for K = 1.6, 400 mA, and a storage-ring energy of 2.4 GeV. Adapted from [8] with permission from John Wiley & Sons.

Importantly, the ratio of the horizontal width of the electron beam to the amplitude of its oscillations induced by the undulator is, for third-generation facilities approximately 100. The reduced horizontal emittance and quasi-on-axis injection of SLS 2.0 produce an electron beam which is significantly narrower, especially in the small-beta short straights occupied by the hard x-ray ID beamlines. Consequently, the ID magnets and poles need only have a width of 15 mm (in contrast to the previous value of 40 mm) to ensure a sufficiently homogeneous magnetic field.

This reduced lateral extent and increased 'elbow room' permits two developments. Firstly, the reduced off-axis excursions of the narrower beam reduces off-axis harmonics and hence these contributions are largely suppressed, as summarised in Figure 7. This narrower electron beam presents several technological opportunities. Firstly, entire undulator maxima can be used for those experiments that do not require a very small relative bandwidth but do require as many photons per unit time on the sample as is possible. At SLS 2.0, these might include certain types of diffraction techniques such as serial crystallography [14–18], lensless imaging that relies primarily on the transverse coherence [12], and imaging techniques such as phase-contrast tomography [19, 20].

Secondly, the reduced oscillations of the electron beam due to the improved injection scheme from the booster means that as it passes along the undulator, the width of the magnets needed to produce a homogeneous field across the central axis can be reduced. The forces acting on the undulator support structure become concomitantly smaller. Moreover, the additional space won by making the magnets narrower also allows the incorporation of two additional sets

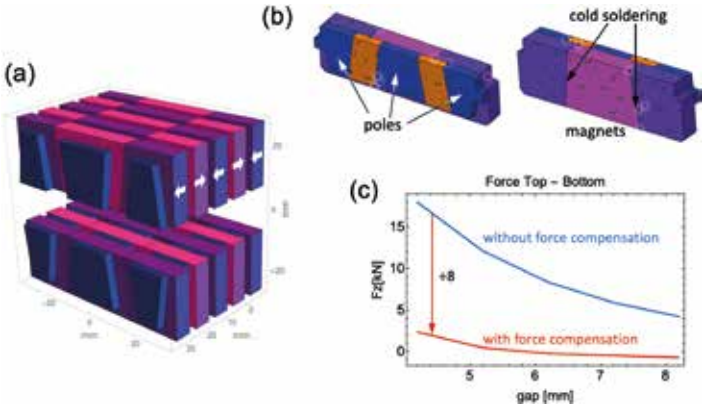

Figure 8. Novel developments in hard x-ray insertion devices. (a) The central Halbach array of poles and magnets can be made to be significantly narrower, thanks to the reduced lateral extent of the electron beam in the orbital plane as it passes through the ID in DLSRs compared to third-generation facilities. Consequently, the forces for a given central magnetic-field strength will be lower. Moreover, the central magnet array can be flanked by arrays in which the poles are opposed (N-N or S-S), thus reducing the total forces even more. The configuration is shown in (b). The reduction in force is typically a factor of eight or more (c), allowing for far more compact and inexpensive mechanical designs. From [9], with permission from the Swiss Society for Photon Science.

of magnets, one on each side of the central array, which, in contrast to the central array, are poled so that they repel (Figure 8). This reduces the net forces on the undulator frame by well over an order of magnitude compared to standard devices used today, and makes them cheaper and much more compact and reliable.

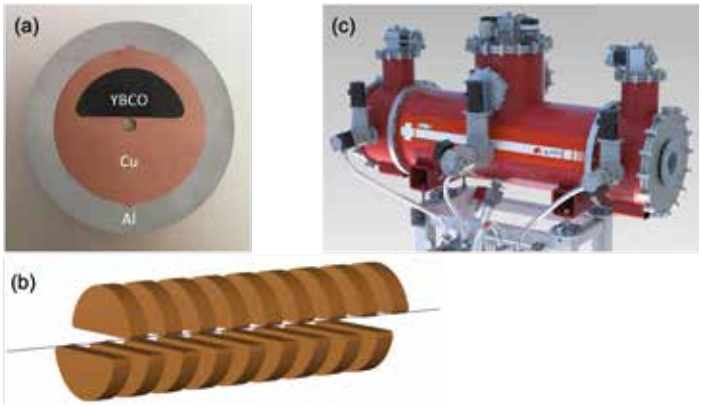

Figure 9. The new HTSU10 superconducting undulator at SLS 2.0. (a) the magnetic elements are half-moons of bulk rare-earth-cuprate superconductors. (b) They are configured in a staggered array to produce the core magnet field. (c) the expunged Meitner field is activated using a 12 T superconducting solenoid in which the HTSC core array is placed.

Another R&D project being pursued concerns a novel insertion device exploiting high-temperature superconducting bulk material (Figure 9). The goal is to generate undulators with ultra-short-period (10.5 mm) and high-strength magnetic fields. Because of the moderate storage-ring energy of SLS 2.0 of 2.7 GeV, high K-values are required in order to enhance the intensities of higher-harmonic radiation, which in turn means that magnetic-field strengths are required that can only be generated using superconducting materials (Equation 11) [21]. For medium-energy synchrotron storage rings such as SLS 2.0, this is a promising route to significantly extend the photon flux to energies beyond 50 keV [Figure 6(c)]. The so-called 'HTSU10', with a 1-m magnetic length, will be installed at the new I-TOMCAT beamline in the second planned shutdown [22].

B. Soft x-ray undulators

The brilliance curves for the soft x-ray insertion devices are shown in Figure 6(b).

The APPLE X undulator design was adopted and developed for the SwissFEL Athos beamline. These insertion devices provide an identical photon-energy range in all major polarization modes (linear horizontal, linear vertical, and circular), with full symmetry over the entire range. This is achieved by using independently controllable radial and longitudinal movements for all four magnet arrays. The radial design is suited to small, round, vacuum chambers used in FELs or other single-pass accelerators, and, importantly, also to DLSRs such as SLS 2.0. By exploiting the latest grade of permanent-magnet material, the magnetic period length can be significantly reduced, which means that the desired soft x-ray photon-energy range can be covered by the fundamental harmonic alone. Undulators with many periods and high magnetic fields are, however, problematic because of the associated high and variable heat load on x-ray optical components. High heat loads require aggressive active cooling solutions that can induce unwanted vibrations that are deleterious to ultimate spectral resolutions and, in the case of micro- and nanofocussing and scanning techniques, also spatial resolution.

The so-called 'APPLE knot' design [23, 24] will be used at ADRESS (UE36kn), QUEST/XIL (UE36kn and UE90kn), and SIM (2 × UE36kn). This 'knot' concept features an additional subharmonic field component (with a period three times longer than that of the main undulator period, see Figure 10). With this magnetic configuration, only the fundamental has its maximum intensity on axis, while the higher harmonics have a cone-like form and are shifted outwards to larger angles. They therefore have a ring-like power-density cross-section. As the fundamental covers the desired energy range for these beamlines, these higher harmonics can then be blocked in the front end using a water-cooled aperture. The load on the optics (mirrors and monochromators) in terms of power density is therefore reduced by a factor of approximately 4, depending on the photon-energy range, allowing more modest cooling and significantly reduced associated vibrations of critical x-ray optical components.

IV. SLS 2.0 Beamline Portfolio and Science Program

The future scientific mission of photon science at SLS will be founded firmly on already established fields of excellence at the Paul Scherrer Institute (PSI). Among others, the SLS to date has produced world-leading research in activities as varied as scanning lensless imaging (ptychographic

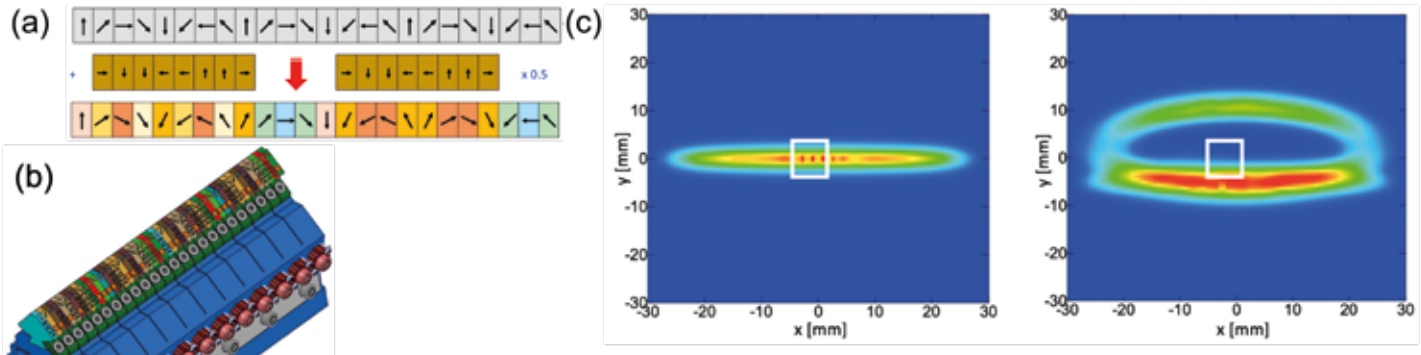

Figure 10. Knot-undulators. (a) Magnet-configuration concept. (b) A single superperiod installed in a jaw of an APPLE-X knot device. (c) Power distribution of the UE90kn in periodic (left) and knot (right) mode 13 m away from the middle of the undulator. The higher harmonics are emitted off-axis, allowing an effective reduction of the heat load inside the bounds of the front-end aperture, marked with the white square.

tomography), diffraction of macromolecular molecules, full-field tomography, soft x-ray angular-resolved photoelectron spectroscopy (ARPES), and resonant inelastic x-ray scattering (RIXS). All of these techniques will profit considerably from the upgrade, which we summarise in this section.

An overview of the beamlines planned for SLS 2.0 is shown in Figure 11.

The main upgrade phase, or 'dark time', to dismantle the existing storage ring and to install the new ring began on 30th September 2023 and will continue until December 2024. For resource reasons, the beamline upgrades have been divided into two phases; first pilot users after the first phase are expected in the Summer of 2025, followed by a further shutdown at the beginning of 2026 and pilot users in Summer 2026.

All already existing beamlines are undergoing upgrades, especially regarding their optics. Moreover, some beamlines have moved, and there are two entirely new beamlines. Changes beyond optics and endstation upgrades include:

- Debye: a new chemistry-focused, hard x-ray spectroscopy/scattering beamline, a sister to the SuperXAS beamline, has already been built.
- I-TOMCAT: a new tomography undulator beamline utilizing the novel HTSU10 is being constructed in Straight 2S, and is complementary to the upgraded TOMCAT beamline, now called S-TOMCAT because of the upgrade of its superbend source from 2.9 T to 5 T.
- The PEARL beamline will amalgamate with the SIS beamline at Straight 9L to create the new QUEST beamline.
- PXIII has been completely rebuilt with new optics and experimental hutches.
- microXAS moves from Straight 5L (which has, in SLS 2.0, an electron beam cross-section incompatible with hard x-ray undulators) to Straight 8S.

Most of the beamlines will benefit from a significant optics upgrade program. The hard x-ray monochromators and mirrors will be redesigned with the reduced horizontal breadth of the photon beam at SLS 2.0 in mind. New crystal and multilayer monochromators will scatter and disperse the incident radiation in the horizontal plane; the minor loss in intensity due to polarization factors will be more than offset by the benefit of horizontal rotational movements, allowing more compact and stable designs. Horizontally deflecting and focusing mirrors will also be able to be made significantly shorter and thereby gain in stability.

V. Concluding Remarks

Electron-accelerator photon sources have a remarkable track record in science, technology and biomedicine. The SLS has been a leading player in this field since the turn of the century. The underlying physics as well as a demand for seeing matter at the atomic and nanoscale ensure that synchrotrons will continue to be essential for scientific and technical progress in the future. Therefore, most third-generation electron storage rings are either considering or actively undergoing an upgrade to a DLSR. At the Paul Scherrer Institute, the plans for the upgraded SLS 2.0 extend beyond simple improvements of the emittance (and thereby also the brilliance), including novel magnet-lattice elements and x-ray sources pioneered at the PSI, plus an aggressive x-ray optics and endstation upgrade program [25]. This will maintain the pre-eminence of PSI, the ETH Domain, and Switzerland in photon science, which has been established by the current SLS and SwissFEL for the foreseeable future.

The machine upgrade [11] in conjunction with novel source technologies will increase the most relevant experimental parameters at the endstations by well over two orders of magnitude in the hard x-ray regime (Figure 12), which will have very substantial benefits to many methods [25], including ptychography [13], full-field tomography [19, 20], macromolecular crystallography [14, 15], soft x-ray ARPES [26], and resonant inelastic x-ray scattering [27].

Indeed, even greater improvements by up to another factor of 100 are anticipated through adaptations in x-ray optics, most notably in the use of multilayer monochromators in stead of crystal monochromators at hard x-ray beamlines, and the substitution of hitherto more conventional but lossy refractive and diffractive focussing elements such as compound refractive lenses and Fresnel zone plates with reflecting elements such as Kirkpatrick-Baez mirrors, which can be made to be more compact than previously possible, thanks to the reduced source sizes.

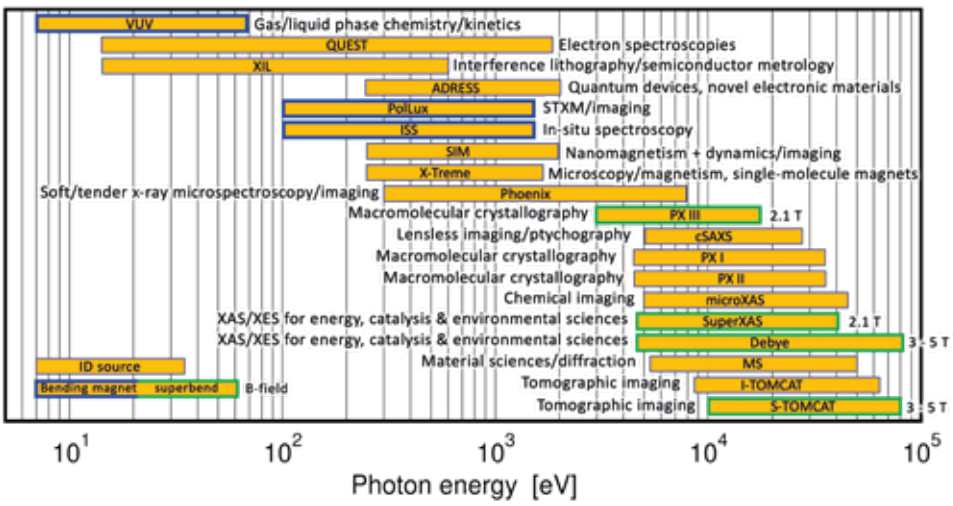

Figure 11. Overview of beamlines in user operation after the upgrade. The source type, the beamline name, areas of major applications, and energy range are shown.

The design, construction and exploitation of SLS 2.0 will enable not only advanced research and education, but also the continued excellence of technology transfer demonstrated by SLS these last two decades, especially in partnership with InnovAare, the node of the Swiss Innovation Park, located next to SLS 2.0.

SLS 2.0 has been designed to be highly synergistic with SwissFEL [28], co-located at PSI, to create a unique centre for accelerator-based photon science in Switzerland. The people and expertise which enabled the recent completion of SwissFEL

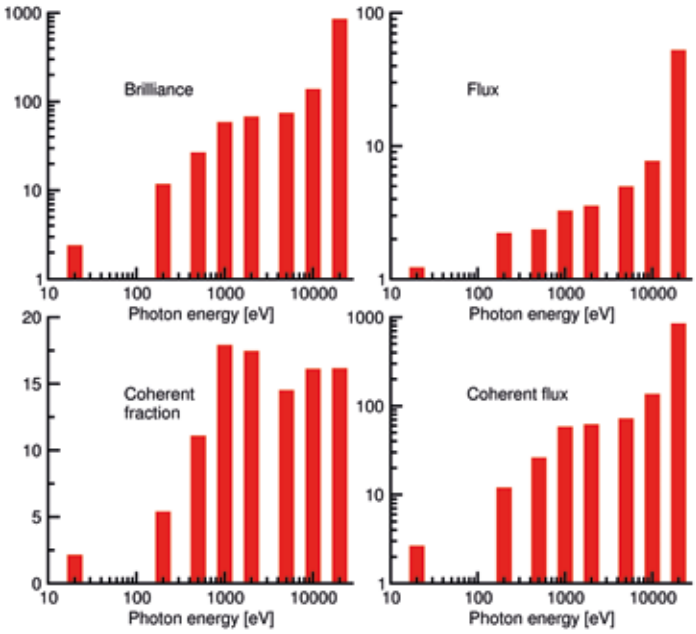

Figure 12. Improvement factors in brilliance, flux, coherent fraction, and coherent flux for the SLS 2.0 upgrade compared to the present SLS, with the new storage-ring energy of 2.7 GeV, for selected photon energies. The undulators assumed in the original SLS are UE212 (8.4 m) for 20 and 200 eV, UE56 (3.6 m) for 500, 1000, and 2000 eV, and U19 (1.8 m) for higher photon energies. The corresponding undulators in SLS 2.0 are UE90 (4.4 m), UE36 (4.4 m), and CPMU15 (3 m).

are now deployed for SLS 2.0. Many of the technologies developed for the SwissFEL project, ranging from serial crystallography to APPLE-X undulators, are now being exported to SLS 2.0; we expect similar fertilization of the Porthos upgrade of SwissFEL which will follow SLS 2.0.

Acknowledgements

Many thanks go to the PSI staff who contributed to the building and operation of the SLS and the planning for the SLS 2.0 project, from the accelerator department, through support and logistics, IT, to the many beamline staff and the user community. Special thanks go to Alun Ashton, Romain Ganter, Juri Honegger, Markus Jörg, Roland Kobler, Frithjof Nolting, Jörg Raabe, Thomas Schmidt, Andreas Streun, Johan Wickström, and Elmar Zehnder for their intimate involvement in the project.

References

[1] M. Selmer, C. M. Dunham, F. V. Murphy IV, A. Weixlbaumer, S. Petry, A. C. Kelley, J. R. Weir, and V. Ramakrishnan. Structure of the 70S ribosome complexed with mRNA and tRNA. *Science*, **313**:1935, 2006.
[2] A. Weixlbaumer, H. Jin, C. Neubauer, R. M. Voorhees, S. Petry, A. C. Kelley, and V. Ramakrishnan. Insights into translational termination from the structure of RF2 bound to the ribosome. *Science*, **322**:953–956, 2008.
[3] R. M. Voorhees, A. Weixlbaumer, D. Loakes, A. C. Kelley, and V. Ramakrishnan. Insights into substrate stabilization from snapshots of the peptidyl transferase center of the intact 70S ribosome. *Nat. Struct. Mol. Biol.*, **16**:528–533, 2009.
[4] M. Jinek, F. Jiang, D. W. Taylor, S. H. Sternberg, E. Kaya, E. Ma, C. Anders, M. Hauer, K. Zhou, S. Lin, M. Kaplan, A. T. Iavarone, E. Charpentier, E. Nogales, and J. A. Doudna. Structures of Cas9 endonucleases reveal RNA-mediated conformational activation. *Science*, **343**:1247997, 2014.
[5] W. Joho, P. Marchand, L. Rivkin, and A. Streun. Design of a Swiss Light Source (SLS). In *Proceedings of the 4th European Particle Accelerator Conference (EPAC1994)*, Proceedings of the European Particle Accelerator Conference, pages 627–629, Singapore, 1994. World Scientific.
[6] J. Bengtsson, W. Joho, P. Marchand, L. Rivkin, and A. Streun. Status of the Swiss Light Source Project SLS. In *Proceedings of the 5th European Particle Accelerator Conference (EPAC1996)*, Proceedings of the European Particle Accelerator Conference, pages 685– 687, London, UK, 1996. Institute of Physics.
[7] M. Eriksson, L. J. Lindgren, M. Sjostrom, E. Wallen, L. Rivkin, and A. Streun. Some small-emittance lightsource lattices with multibend achromats. *Nucl. Instrum. Methods A*, **587**:221, 2008.
[8] P. R. Willmott. *Introduction to Synchrotron Radiation – Techniques and Applications.* John Wiley and Sons, 2nd edition, 2019.
[9] P. R. Willmott, G. Aeppli, A. Ashton, C. Bostedt, O. Bunk, M. Calvi, Y. Ekinci, U. Flechsig, R. Ganter, T. Garvey, M. Jörg, D. Just, R. Kobler, F. Nolting, L. Patthey, C. Pradervand, J. Raabe, L. Rivkin, B. Rösner, T. Schmidt, A. Streun, F. van der Veen, and H. Braun. The Swiss Light Source Upgrade to a Diffraction-Limited Storage Ring. *Swiss Society for Photon Science Newsletter*, **2**:2–12, 2022.
[10] M. Aiba, A. Anghel, U. Barth, M. Böge, C. Calzolaio, M. Calvi, A. Citterio, M. Dehler, K. Dreyer, T. Garvey, C. Gough, M. Hahn, D. Hauenstein, J. Honegger, B. Keil, P. Lerch, S. Maag, F. Marcellini, M. Negrazus, B. Ronner, S. Sanfilippo, C. Sattler, V. Schlott, T. Schmidt, L. Schulz, L. Stingelin, A. Streun, V. Vrankovic, J. Wickström, A. Wrulich, E. Zehnder, and E. Zimoch. SLS-2 Conceptual Design Report. Technical report, Paul Scherrer Institute, 2017.
[11] H. Braun et al. SLS 2.0 storage ring. Technical design report. Technical report, Paul Scherrer Institute, 2021.
[12] F. Pfeiffer. X-ray ptychography. *Nature Photonics.*, **12**:9–17, 2018.
[13] M. Guizar-Sicairos and P. Thibault. Ptychography: A solution to the phase problem. *Physics Today*, **74**:42–48, 2021.
[14] S. Botha, K. Nass, T. R. M. Barends, W. Kabsch, B. Latz, F. Dworkowski, L. Foucar, E. Panepucci, M. Wang, R. L. Shoeman, I. Schlichting, and R. B. Doak. Room-temperature serial crystallography at synchrotron x-ray sources using slowly flowing freestanding high-viscosity microstreams. *Acta Crystallogr. D*, **71**:387–397, 2015.
[15] P. Nogly, D. James, D. Wang, T. A. White, N. Zatsepin, A. Shilova, G. Nelson, H. Liu, L. Johansson, M. Heymann, K. Jaeger, M. Metz, C. Wickstrand, W. Wu, P. Bath, P. Berntsen, D. Oberthuer, V. Panneels, V. Cherezov, H. Chapman, G. Schertler, R. Neutze, J. Spence, I. Moraes, M. Burghammer, J. Standfuss, and U. Weierstall. Lipidic cubic phase serial millisecond crystallography using synchrotron radiation. *IUCrJ*, **2**:168–176, 2015.
[16] F. Stellato, D. Oberthür, M. Liang, R. Bean, C. Gati, O. Yefanov, A. Barty, A. Burkhardt, P. Fischer, L. Galli, R. A. Kirian, J. Meyer, S. Panneerselvam, C. H. Yoon, F. Chervinskii, E. Speller, T. A. White, C. Betzel, A. Meents, and H. N. Chapman. Room-temperature macromolecular serial crystallography using synchrotron radiation. *IUCrJ*, **1**:204–212, 2014.
[17] C. Gati, G. Bourenkov, M. Klinge, D. Rehders, F. Stellato, D. Oberthür, O. Yefanov, B. P. Sommer, S. Mogk, M. Duszenko, C. Betzel, T. R. Schneider, H. N. Chapman, and L. Redecke. Serial crystallography on in vivo grown microcrystals using synchrotron radiation. *IUCrJ*, **1**:87–94, 2014.
[18] K. Diederichs and M. Wang. Serial synchrotron x-ray crystallography (SSX). *Methods Mol. Biol.*, **1607**:239– 272, 2017.
[19] T. J. Davis, D. Gao, T. E. Gureyev, A. W. Stevenson, and S. W. Wilkins. Phase-contrast imaging of weakly absorbing materials using hard x-rays. *Nature*, **373**:595– 598, 1995.
[20] A. Momose, T. Takeda, Y. Itai, and K. Hirano. Phase-contrast x-ray computed tomography for observing biological soft tissues. *Nature Med.*, **2**:473–475, 1996.
[21] M. Calvi, M. D. Ainslie, A. Dennis, J. H. Durrell, S. Hellmann, C. Kittel, D. A. Moseley, T. Schmidt, Y. Shi, , and K. Zhang. A GdBCO bulk staggered array undulator. *Supercond. Sci. Technol.*, **33**:014004, 2020.
[22] K. Zhang, A. Pirotta, X. Liang, S. Hellmann, M. Bartkowiak, T. Schmidt, A. Dennis, M. Ainslie, J. Durrell, and M. Calvi. Record field in a 10 mm-period bulk high-temperature superconducting undulator. *Supercond. Sci. Technol.*, **36**:05LT01, 2023.
[23] S. Sasaki, A. Miyamoto, and S. Qiao. Design study of KNOT-APPLE undulator for PES-Beamline at SSRF. *Proc. PAC2013*, pages 1043–1054, 2013.
[24] F. Ji, R. Chang, Q. Zhou, W. Zhang, M. Ye, S. Sasaki, and S. Qiao. Design and performance of the APPLE-Knot undulator. *J. Synchrotron Rad.*, **22**:901–907, 2015.
[25] P. R. Willmott et al. SLS 2.0 Beamline Conceptual Design Report. Technical report, Paul Scherrer Institute, 2021.
[26] L. L. Lev, I. O. Maiboroda, M. A. Husanu, E. S. Grichuk, N. K. Chumakov, I. S. Ezubchenko, I. A. Chernykh, X. Wang, B. Tobler, T. Schmitt, M. L. Zanaveskin, V. G. Valeyev, and V. N. Strocov. k-space imaging of anisotropic 2D electron gas in GaN/GaAlN high-electron-mobility transistor heterostructures. *Nat. Comms.*, **9**:2653, 2018.
[27] L. J. P. Ament, M. van Veenendaal, T. P. Devereaux, J. P. Hill, and J. van den Brink. Resonant inelastic x-ray scattering studies of elementary excitations. *Rev. Mod. Phys.*, **83**:705–767, 2011.
[28] F. Nolting, C. Bostedt, T. Schietinger, and H. Braun. The Swiss Light Source and SwissFEL at the Paul Scherrer Institute. *Eur. Phys. J. Plus*, **138**:126, 2023.